



# 3D structure of nano-oriented crystals of poly(ethylene terephthalate) formed by elongational crystallization from the melt

Kiyoka Okada<sup>1</sup> · Yoshitaka Tanaka<sup>2</sup> · Hiroyasu Masunaga<sup>3</sup> · Masamichi Hikosaka<sup>1</sup>

Received: 9 August 2017 / Revised: 27 September 2017 / Accepted: 30 September 2017 / Published online: 14 December 2017  
© The Society of Polymer Science, Japan 2018

## Abstract

We studied the elongational crystallization of poly(ethylene terephthalate) (PET) from the melt using polarizing optical microscope and X-ray observation. We verified that the structure and morphology discontinuously changed from conventional stacked lamellae of folded chain crystals (FCCs) to nano-oriented crystals (NOCs) when the elongational strain rate ( $\dot{\epsilon}$ ) exceeded a critical value of ( $\dot{\epsilon}^*$ )  $\cong 10^2 \text{ s}^{-1}$ . Therefore, the universality of NOC formation was verified. We found that the NOCs of PET show a novel three-dimensional (3D) structure and morphology: (i) nanocrystals (NCs) were arranged in a monoclinic lattice, which is a specific morphology for NOCs of PET, compared to iPP, and (ii) the unit cell structure of NOCs was a triclinic system with biaxial orientation. We showed the important role of the primary structure of the plate, such as a benzene ring, in the formation of a novel 3D structure and the morphology of the NOCs of PET. We also clarified that the NOCs of PET showed high performance, such as a high heat resistance temperature ( $T_h$ )  $\cong 281 \text{ }^\circ\text{C}$ , a high melting temperature ( $T_m$ )  $\cong 285 \text{ }^\circ\text{C}$ , high maximum tensile stresses for the machine direction (MD) and transverse direction (TD)  $\cong 2.8 \times 10^2$  and 74 MPa, respectively, and high Young's moduli for MD and TD  $\cong 5.4$  and 1.7 GPa, respectively.

## Introduction

We found that the elongational crystallization from the supercooled melt of isotactic polypropylene (iPP) results in the formation of a novel morphology of “nano-oriented crystals (NOCs)” [1]. The NOCs were formed when the elongational strain rate ( $\dot{\epsilon}$ ) surpassed a critical level ( $\dot{\epsilon}^*$ ), where  $\dot{\epsilon}^*$  is defined as the  $\dot{\epsilon}$  where the volume fraction of NOCs [ $f(\text{NOC})$ ] exceeds 0.6 [1]. Using a polarizing optical microscope (POM) and small/wide angle X-ray scattering (SAXS/WAXS), we observed that the structure and morphology of NOCs showed a one-dimensional (1D) orientation. We clarified that nanocrystals (NCs) were arranged as a paracrystal

[2] along the elongational direction and that the molecular entanglements originally included within the melt should be condensed to the interface between NCs. We determined the size of an NC ( $d$ ) from a two-point pattern of SAXS. Here, we assumed that the distance between the nearest neighbors is approximately equal to  $d$  due to high crystallinity.

We showed that  $\dot{\epsilon}^*$  increased with the increase in crystallization temperature ( $T_c$ ). We clarified that NOC formation is mainly controlled by the nucleation process using the following facts [1, 3]. We showed that the degree of supercooling ( $\Delta T$ ) dependence of the nucleation rate ( $I$ ) of NOCs satisfied the theoretical equation of classical nucleation theory,  $I \propto \exp[-C/\Delta T^2]$  for homogeneous nucleation, where  $C$  is a constant and  $\Delta T$  is defined by  $\Delta T \equiv T_m^0 - T_c$ , where  $T_m^0$  is the equilibrium melting temperature [4]. We proposed the formation model of NOCs from the oriented melt. We estimated  $T_m^0$  for the oriented melt for iPP [3].

The NOCs showed high performance, including high thermal resistance and high tensile strength. Here, we defined the heat resistance temperature ( $T_h$ ) as the temperature where thermal strain ( $\epsilon'$ ) exceeds 13% with an increase in temperature ( $T$ ) [1]. Here,  $\epsilon'$  is defined by

$$\epsilon' \equiv \frac{l' - l_0}{l_0}, \quad (1)$$

✉ Masamichi Hikosaka  
hikosaka@hiroshima-u.ac.jp

<sup>1</sup> Graduate School of Integrated Arts and Sciences, Hiroshima University, 1-7-1 Kagamiyama, Higashi Hiroshima-shi, Hiroshima 739-8521, Japan

<sup>2</sup> Film Research Section, Teijin Film Solutions Limited, 1357 Minamijo, Anpachi-cho, Anpachi-gun, Gifu 503-0123, Japan

<sup>3</sup> SPring-8, Japan Synchrotron Radiation Research Institute (JASRI), 1-1-1 Kouto, Sayo-cho, Sayo-gun, Hyogo 679-5198, Japan

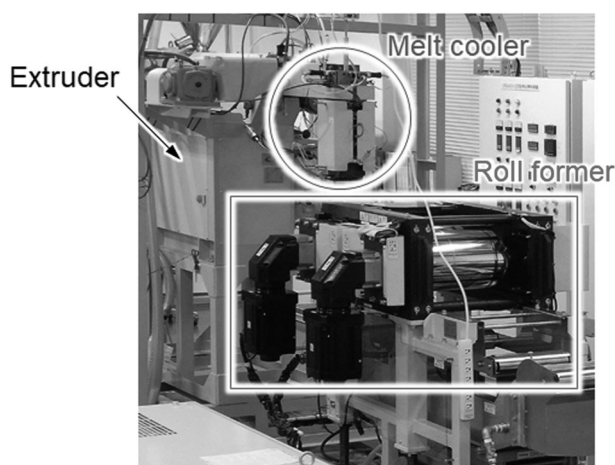


**Fig. 1** Roll-type apparatus for 1D elongational crystallization. Extruder, melt cooler and roll former. (Color figure online)

where  $l'$  is lateral length and  $l'_0$  is initial lateral length at room temperature.

Therefore, it is scientifically interesting and important to show the universality of NOC formation for other crystalline polymers to clarify the formation mechanism of NOCs in the elongational crystallization and show high performance.

In this study, we will focus on poly(ethylene terephthalate) (PET) as a typical polyester. PET is widely used, is recyclable, and shows higher thermal resistance, higher tensile strength, and higher chemical resistance than polyolefin. In the case of crystallized PET samples obtained using a conventional molding method, the morphology consists of stacked lamellae composed of folded chain crystals (FCCs) and amorphous material. We will show in this paper that the unit cell structure of NOCs is triclinic [5]. The crystallinity is low. The melting temperature ( $T_m$ ) and  $T_h$  are relatively low.  $T_m^0$ s are reported as follows. Ikeda et al. showed that  $T_m^0 = 284^\circ\text{C}$  using a Hoffman-Weeks plot [6]. Fakirov et al. showed  $T_m^0 = 310^\circ\text{C}$  using a Gibbs-Thomson plot [7]. Mehta et al. showed  $T_m^0 = 280^\circ\text{C}$  by thermal analysis [8]. Dörscher et al. showed  $T_m^0 = 282^\circ\text{C}$  according to the theory of Flory and Vrij [9]. Here, we will use  $T_m^0 = 310^\circ\text{C}$ ; [7] the reason is shown in the RESULTS.

Since PET includes a plate-like benzene ring within a main polymer chain as a primary structure, the role of the benzene ring in the elongational crystallization should be an interesting problem. We can verify the universality of NOC formation by showing the formation of NOCs of PET and the formation mechanism of NOCs. In addition, we expect that NOC formation will realize much higher performance of PET as a homopolymer, but not as composite materials.

The purposes of this study are (1) to verify the universality of NOC formation using PET when  $\dot{\epsilon}$  becomes larger than  $\dot{\epsilon}^*$ ; (2) to clarify the three-dimensional (3D)

structure and morphology of NOCs of PET; and (3) to demonstrate that the PET NOCs show high performance.

## Materials and methods

### Material

We used PET (Teijin Ltd.,  $M_w = 79.7 \times 10^3$ ,  $M_w/M_n = 2.22$ ), where  $M_w$  is the weight-averaged molecular weight,  $M_n$  is the number-averaged molecular weight, and  $M_w/M_n$  is the index of dispersion.

### Elongational crystallization condition

We used a roll-type apparatus for 1D elongational crystallization (Fig. 1) [1]. The pellets were first melted within an extruder at the maximum temperature  $T_{\max} = 320^\circ\text{C}$ , which is higher than  $T_m^0$ , and then cooled to  $T_c$  using a handmade “melt cooler” to obtain the supercooled melt. The supercooled melt was rolled to elongate it into a sheet. The radius of a pair of rotating rolls ( $R_{\text{roll}}$ ) was 125 mm. The range of  $T_c$  was  $(232\text{--}245)^\circ\text{C}$ . The temperature of the roll surface was also controlled at the same  $T_{cs}$ . The gap between rolls changed from 0.15 to 0.55 mm. The range of  $\dot{\epsilon}$  was  $(0\text{--}4.1 \times 10^2) \text{ s}^{-1}$ . In the case of a roll-type apparatus,  $\dot{\epsilon}$  is given by

$$\dot{\epsilon} = V_R / \sqrt{R_{\text{roll}} L_{\text{obs}}}, \quad (2)$$

where  $V_R$  is the surface velocity of the rotating roll and  $L_{\text{obs}}$  is the sheet thickness after elongational crystallization.  $L_{\text{obs}}$  was  $\sim(0.23\text{--}0.71) \text{ mm}$ . The formula for Eq. 2 is shown in the APPENDIX. In the case of a compression-type apparatus, the formulation of  $\dot{\epsilon}$  is shown in ref. 1.

We determined  $\dot{\epsilon}^*$  using a POM, SAXS, and WAXS according to the method shown in ref. 1. We denote “Quiescent (Q)”,  $\dot{\epsilon}(S)$ ,  $\dot{\epsilon}(M)$ , and  $\dot{\epsilon}(L)$  as  $\dot{\epsilon} = 0 \text{ s}^{-1}$ ,  $\dot{\epsilon} \ll \dot{\epsilon}^*$ ,  $\dot{\epsilon} < \dot{\epsilon}^*$ , and  $\dot{\epsilon} \geq \dot{\epsilon}^*$ , respectively. The directions for the sheet sample are as follows: the machine direction (MD) is the direction of melt elongation; the transverse direction (TD) is the direction of the sheet width; and the normal direction (ND) is the direction of sheet thickness.

### Crystallization under a quiescent field

We used a PET sample to observe crystallization under a quiescent field as a reference. It was first melted at  $T_{\max} = 320^\circ\text{C}$  for 1 min and was crystallized isothermally at a fixed  $T_c = 241^\circ\text{C}$  for 17 h, which was set to be larger than the solidification time ( $\tau_s$ ).  $\Delta T = 69 \text{ K}$ . Crystallization under a quiescent field was observed using a POM (Nikon, OPTIPHOT2-POL) and a hot stage (Mettler Toledo, FP90 and

FP87HT) and was recorded using a CCD camera (Nikon, DS-Ri1).

First, we sandwiched a small amount of PET sample between two cover glasses. The thickness of the sample was  $\sim 16 \mu\text{m}$ . The sample was placed on a hot stage. The POM was arranged in a crossed nicols.

## Instruments

The optical morphology of the sample was observed using a POM (Olympus, BX51N-33P-OC) and a CCD camera system (Olympus, DP25). We arranged the POM in crossed nicols and inserted the sensitive color plate (scp). We sliced the samples crystallized by melt elongation at a thickness of (20–50)  $\mu\text{m}$  for morphological observations. We qualitatively observed the orientation of the molecular chain from the retardation ( $R$ ).

SAXS and WAXS observations were performed using synchrotron radiation at the beam line BL03XU of SPring-8 of the Japan Synchrotron Radiation Research Institute (JASRI). The wavelength was (0.06–0.15) nm, the camera length was (0.3–3) m, and we used the imaging plate as a detector. We obtained the SAXS and WAXS intensities of the sample by correcting the background intensity.

We observed a sample along the “through”, “edge”, and “end” directions using a POM, SAXS, and WAXS. Here, “through” is parallel to ND, which is also the compressed direction, “end” is parallel to MD, i.e., the elongational direction, and “edge” is parallel to TD, which is perpendicular to the “through” and “end” directions.

## Density $\rho$

The density ( $\rho$ ) was obtained by using a density gradient tube method of direct reading. The specific gravity was precisely measured using a density-measuring system (Shibayama scientific Co. Ltd., Type A) at 23 °C. We used calcium nitrate and ion water to obtain light and heavy solutions. The range of specific gravity was (1.40–1.56)  $\text{g}/\text{cm}^3$ .

## Analysis method

The orientation function ( $f_c$ ) is a well-known order parameter that expresses the degree of chain orientation [10]. We measured  $f_c$  using the half-width of the 010 reflection of the triclinic unit cell structure.

$f(\text{NOC})$  was obtained from POM or X-ray observations [1]. We obtained  $f(\text{NOC})$  easily using a POM in this study from a cross-section of a sample, including edge-view and end-view observations.  $f(\text{NOC})$  is defined by

$$f(\text{NOC}) \equiv (L_{\text{obs}} - L_{\text{center}})/L_{\text{obs}}, \quad (3)$$

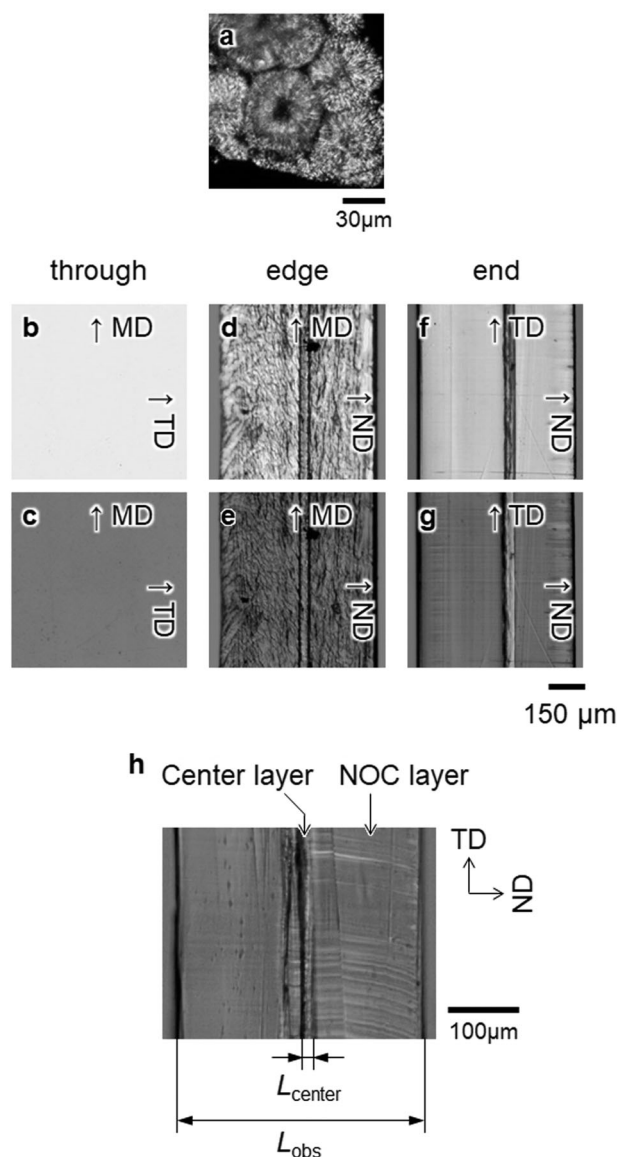


**Fig. 2** Optical morphology obtained by a POM. **a** Sample crystallized under a quiescent field.  $T_c = 241 \text{ }^\circ\text{C}$ . Scale bar is 30  $\mu\text{m}$ . **b–g** Sample of  $\dot{\epsilon}(L)$  for through, edge, and end-views.  $T_c = 241 \text{ }^\circ\text{C}$  and  $\dot{\epsilon} = 3.2 \times 10^2 \text{ s}^{-1}$ . Scale bar is 150  $\mu\text{m}$ . **b, d** MD//scp. **f** TD//scp. **c, e, g** Extinction angle. **h** Sample of  $\dot{\epsilon}(L)$  at extinction angle for end-view.  $T_c = 232 \text{ }^\circ\text{C}$  and  $\dot{\epsilon} = 2.6 \times 10^2 \text{ s}^{-1}$ . Scale bar is 50  $\mu\text{m}$ . Center layer is sandwiched by NOC layers. (Color figure online)

where  $L_{\text{center}}$  is the thickness of the “center layer” within a sample. The detailed description of the center layer will be shown in the RESULTS.

## Physical properties

A thermal resistance test was performed using a hot stage (Linkam Scientific Instruments Ltd., L-600A) and a POM and was recorded using a CCD camera. Square-cut samples were placed on the hot stage and heated from room

temperature to 327 °C at a heating rate of 1 K/min. We observed the  $\varepsilon$ 's from  $l_s$  along the MD and TD of the sample and designated them as  $\varepsilon'_{MD}$  and  $\varepsilon'_{TD}$ , respectively.

Tensile properties were tested using a tension tester (Shimazu, Autograph AG-1kNIS) [1]. The tensile properties were observed at room temperature with a strain rate of  $0.2 \text{ s}^{-1}$ . We observed the stress ( $\sigma$ ) and strain ( $\varepsilon^\dagger$ ) and obtained the maximum tensile stress ( $\sigma_{\max}$ ) and Young's modulus ( $E_t$ ).

## Results

### Optical morphology and crystallization

#### Optical morphology

We show the typical optical morphology of Q for  $T_c = 241 \text{ °C}$  and a through-view via a POM in Fig. 2a. Large spherulites were generated. The mean diameter of the spherulites was  $\sim 56 \text{ }\mu\text{m}$ .

We show the typical morphology of  $\dot{\varepsilon}(L)$  for  $T_c = 241 \text{ °C}$  in Figs. 2b–g. The through-view showed the high orientation of the molecular chains along MD (Figs. 2b, c).  $R$  was yellow when MD was parallel to the scp, i.e.,  $MD//scp$  ( $\pi/4$ ) and  $MD \perp scp$  ( $3\pi/4$ ), and was purplish red at the extinction angle ( $0$  and  $\pi/2$ ). Therefore, the formation of NOCs was suggested. The morphology of the edge-view showed “NOC layers” and a “center layer” that was sandwiched by the NOC layers. The  $R$ s of NOC layers were yellow and purplish red at  $MD//scp$  and extinction angles, respectively (Figs. 2d, e). Therefore, we recognized that NOCs were formed in this layer. However, the  $R$  of the central layer showed an unoriented color. Thus, we found that NOCs were not formed in the central layer, which we named the “center layer”. The end-view also showed a sandwiched morphology of NOC layers and the center layer (Figs. 2f, g). The  $R$ s of NOCs layers were purplish red at the extinction angle and yellow when TD was parallel to the scp, i.e.,  $TD//scp$ . This means that the  $R$  of the end-view [ $R(\text{end})$ ] for PET is not 0, i.e.,

$$R(\text{end}) \neq 0 \text{ for PET.} \quad (4)$$

On the other hand,  $R(\text{end})$  for iPP was 0 [1],

$$R(\text{end}) = 0 \text{ for iPP} \quad (5)$$

No references include the refractive index ( $n$ ) of PET to our knowledge, but it appears that  $n_a \neq n_b$ , where  $n_a$  and  $n_b$  are the  $n$ s for the  $a$ -axis and  $b$ -axis, respectively. The crystal size for  $\dot{\varepsilon}(L)$  was too small to detect using a POM. Therefore, the morphology discontinuously changed at  $\dot{\varepsilon}^*$ .

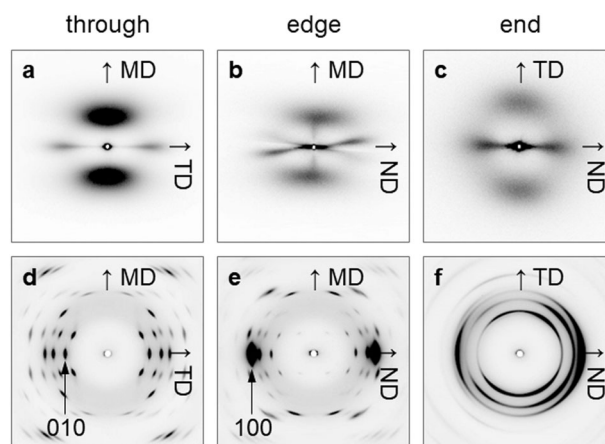


**Fig. 3** X-ray scattering patterns of  $\dot{\varepsilon}(L)$  for through-view, edge-view, and end-views.  $T_c = 241 \text{ °C}$  and  $\dot{\varepsilon} = 3.2 \times 10^2 \text{ s}^{-1}$ . **a–c** SAXS images. **d–f** WAXS images

#### Induction time ( $\tau_i$ ) and solidification time ( $\tau_s$ )

$\tau_s$  for Q was  $\tau_s \cong 15 \text{ h}$  for  $T_c = 241 \text{ °C}$  (6), but that for  $\dot{\varepsilon}(L)$  was  $\tau_s \cong 10 \text{ ms}$  (7) for the same  $T_c$ . This indicates that  $\tau_s$  for  $\dot{\varepsilon}(L)$  was  $5 \times 10^6$  times smaller than that for Q for the same  $T_c$ . Therefore, crystallization for NOCs was accelerated  $\sim 5 \times 10^6$ -fold by melt elongation compared to that under a quiescent field for the same  $T_c$ .

### Morphology and structure

#### Morphology of NOCs according to SAXS

We show a typical SAXS pattern of NOCs for  $T_c = 241 \text{ °C}$  in Figs. 3a–c. The through-view showed a strong two-point pattern along MD and a weak one along TD. These patterns were mutually orthogonal. The edge-view showed novel inclined two-point patterns for MD and ND. The inclined two-point pattern for ND is important to determine the 3D morphology of NOCs, as will be described in DISCUSSION. It also showed a streak along MD and two streaks along ND. With respect to two streaks along ND, one was strong in the direction of a two-point pattern of ND, and the other was weak. Details of the edge-view pattern are shown in the APPENDIX. The end-view showed weak two-point patterns along TD and ND that were mutually orthogonal and also showed a streak along ND.

These novel SAXS patterns clarified the formation of NOCs and provide evidence that NCs are arranged in a 3D lattice. The lattice type of NC should belong to the monoclinic system with a unique axis of TD [11]. Details are shown in DISCUSSION.



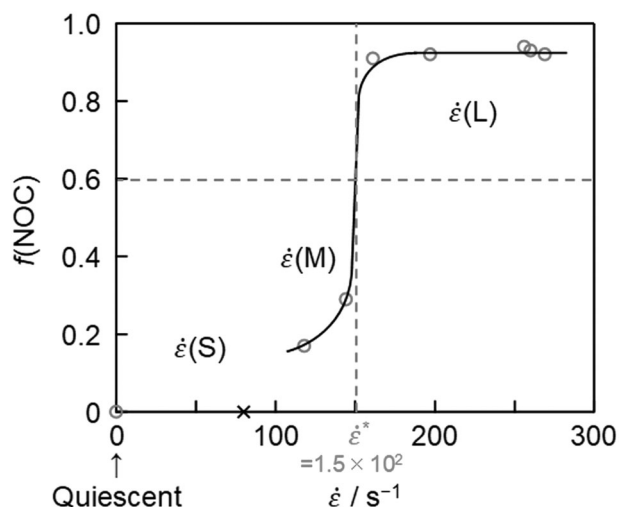


**Fig. 4**  $\dot{\epsilon}$  dependence of  $f(\text{NOC})$  for  $T_c = 232^\circ\text{C}$ . This result indicates that  $\dot{\epsilon}^* = 1.5 \times 10^2 \text{ s}^{-1}$ . (Color figure online)

### Structure of NOCs according to WAXS

We show typical WAXS patterns of NOCs for  $T_c = 241^\circ\text{C}$  in Figs. 3d–f. The crystal lattice belonged to the triclinic system [5]. The through-view showed a highly oriented fiber pattern along MD. The edge-view also showed a highly oriented fiber pattern along MD, and the intensity of the 100 reflection was very strong. The end-view showed a broad biaxially oriented pattern. Crystallinity should be high, as the scattering intensity of the amorphous halo was very weak.

Since the reflections for  $l \geq 1$  are displaced from the normal layer lines (Figs. 3d, e), we clarified that the structure of NOCs should be highly ordered, with molecular chains tilted a few degrees from MD [5, 12].

### Density ( $\rho$ )

The  $\rho$  for  $\dot{\epsilon}(\text{L})$  was  $\rho = 1.406 \pm 0.004 \text{ g/cm}^3$  (8), where  $\rho$  was averaged, including the NOCs and center layers (Fig. 2h). We also obtained  $\rho$  for Q, and  $\rho = 1.420 \pm 0.002 \text{ g/cm}^3$  (9). Hence, the  $\rho$  for  $\dot{\epsilon}(\text{L})$  was almost the same as the  $\rho$  for Q.

### Volume fraction of NOCs, $f(\text{NOC})$

We show a typical optical morphology of  $\dot{\epsilon}(\text{L})$  for the end-view for  $T_c = 232^\circ\text{C}$  in Fig. 2h, from which we obtained  $f(\text{NOC})$  using Eq. 3.

$$f(\text{NOC}) \cong 0.94 \text{ for } \dot{\epsilon}(\text{L}). \quad (10)$$

We show the  $\dot{\epsilon}$  dependence of  $f(\text{NOC})$  in Fig. 4. Here,  $f(\text{NOC}) = 0$  corresponds to a sample of Q. As we were not able to obtain any sheets in the range  $0 < \dot{\epsilon} < 1 \times 10^2 \text{ s}^{-1}$

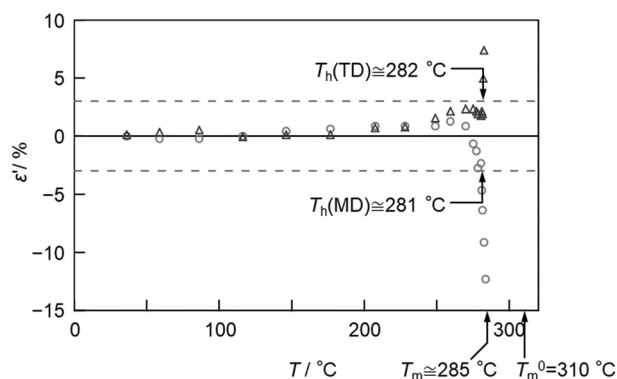


**Fig. 5** Plots of  $\epsilon'$  against  $T$  for NOCs. Circles and triangles correspond to  $\epsilon'$ 's for MD and TD, respectively. (Color figure online)

because of the difficulty of crystallization, there is no plot for  $f(\text{NOC})$ . When  $\dot{\epsilon}$  increased from  $1 \times 10^2$  to  $1.4 \times 10^2 \text{ s}^{-1}$ ,  $f(\text{NOC})$  began to increase from 0.2 to 0.3. For  $\dot{\epsilon} > 1.4 \times 10^2 \text{ s}^{-1}$ ,  $f(\text{NOC})$  significantly increased and saturated to

$$f(\text{NOC}) \cong 1 \text{ for } \dot{\epsilon} \geq 1.6 \times 10^2 \text{ s}^{-1}. \quad (11)$$

Therefore, we concluded that

$$\dot{\epsilon}^* = 1.5 \times 10^2 \text{ s}^{-1}. \quad (12)$$

The center layer was formed because a sheet was compressed and elongated by a pair of rolls. Thus, the specific melt flow in the central zone should be the origin. We can obtain a much thinner center layer when the molded parameters are optimized.

### Orientation function ( $f_c$ ) of the c-axis

We obtained  $f_c$  by analyzing the 010 reflection for a through-view pattern (Fig. 3d).

$$f_c(010) \cong 0.97 \text{ for } \dot{\epsilon}(\text{L}). \quad (13)$$

Therefore, we clarified that the molecular chains for  $\dot{\epsilon}(\text{L})$  were highly oriented along MD.

### Thermal resistance

Figure 5 presents thermal resistance tests for NOCs. We plotted  $\epsilon'$  against  $T$ . When  $T$  increased,  $\epsilon'_{\text{MD}}$  and  $\epsilon'_{\text{TD}}$  increased only slightly up to  $\sim 230^\circ\text{C}$  and then slowly increased above  $230^\circ\text{C}$ .  $\epsilon'_{\text{MD}}$  became smaller than  $-3\%$  above  $281^\circ\text{C}$ , and  $\epsilon'_{\text{TD}}$  became larger than  $3\%$  above  $282^\circ\text{C}$ . The crystal of NOCs melted at  $\sim 285^\circ\text{C}$ . Therefore, we obtained  $T_h$ 's for MD [ $T_h(\text{MD})$ ] and TD [ $T_h(\text{TD})$ ]:

$$T_h(\text{MD}) \cong 281^\circ\text{C}, \quad (14a)$$

$$T_h(\text{TD}) \cong 282^\circ\text{C}, \quad (14b)$$

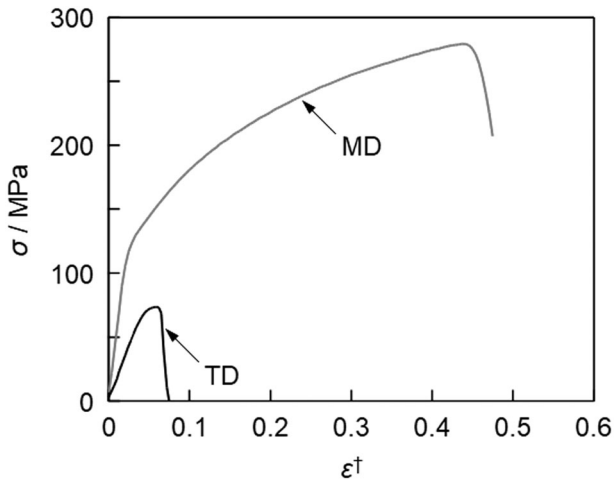


**Fig. 6** Stress ( $\sigma$ ) – strain ( $\epsilon^\dagger$ ) curves for NOCs. Red and black curves correspond to curves for MD and TD, respectively. (Color figure online)

We also obtained the  $T_m$  of NOCs [ $T_m(\text{NOC})$ ],

$$T_m(\text{NOC}) \cong 285^\circ\text{C} \quad (15)$$

It was clarified that  $T_m(\text{NOC})$  was larger than  $T_m^0 = (280\text{--}284)^\circ\text{C}$  [6, 8, 9]. Therefore, we used  $T_m^0 = 310^\circ\text{C}$  in this study.

### Tensile stress and Young's modulus

We show  $\sigma$  vs.  $\epsilon^\dagger$  for  $\dot{\epsilon}(\text{L})$  in Fig. 6. The  $\sigma_{\max}$ s of NOCs for MD and TD were

$$\sigma_{\max} \cong 2.8 \times 10^2 \text{ MPa} \quad (16a)$$

and

$$\sigma_{\max} \cong 7 \text{ MPa}, \quad (16b)$$

respectively.

The  $E_t$ s of NOCs for MD and TD were

$$E_t \cong 5.4 \text{ GPa} \quad (17a)$$

and

$$E_t \cong 1.7 \text{ GPa}. \quad (17b)$$

respectively. Therefore, the  $\sigma_{\max}$  and  $E_t$  of  $\dot{\epsilon}(\text{L})$  showed higher performance than a bulky melt crystallized FCC-PET sample:  $\sigma_{\max} \cong 4 \text{ MPa}$  and  $E_t \cong 2.3 \text{ GPa}$  (18) [13].

## Discussion

### 3D morphology of NCs

#### Reciprocal lattice of NCs

The two-point SAXS patterns for  $\dot{\epsilon}(\text{L})$  are primary peaks, which means that the NCs are arranged in a paracrystal on a

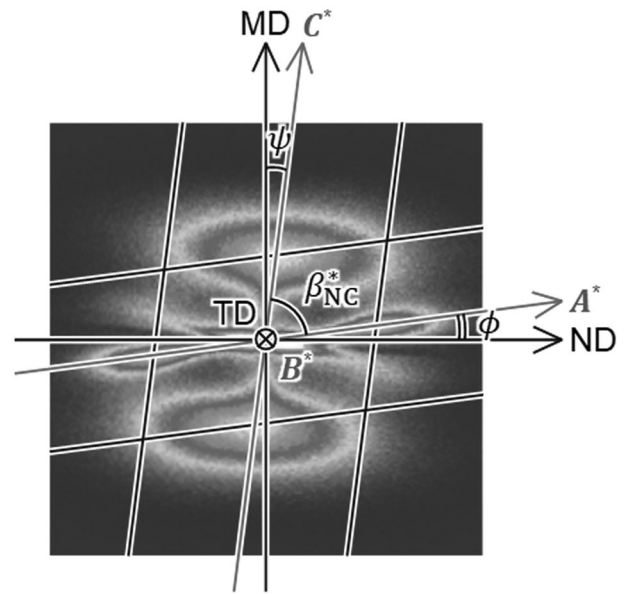


**Fig. 7** Illustration of reciprocal lattice in SAXS image for edge-view.  $T_c = 241^\circ\text{C}$  and  $\dot{\epsilon} = 3.2 \times 10^2 \text{ s}^{-1}$ . The reciprocal lattice type of the NC belongs to the monoclinic system. (Color figure online)

3D lattice [2]. We illustrate the reciprocal lattice projected onto an  $A^*C^*$  plane in Fig. 7, from which we concluded that the reciprocal lattice type of the NC belongs to a monoclinic system, where  $A^*$ ,  $B^*$ , and  $C^*$  are reciprocal lattice vectors of the NC, and  $\beta_{\text{NC}}^*$  is an angle between two-point patterns along MD and ND. The unique axis is  $B^*/\text{TD}$ .  $\psi$  and  $\phi$  are azimuth angles of the NC, counted clockwise from MD and ND, respectively.

We obtained  $\psi = 7.2^\circ$  and  $\phi = -7.5^\circ$  (19).  $\beta_{\text{NC}}^*$  is defined as

$$\beta_{\text{NC}}^* \equiv \pi/2 - \psi - |\phi|. \quad (20)$$

Therefore, we obtained

$$\beta_{\text{NC}}^* = 75.3^\circ. \quad (21)$$

#### Monoclinic lattice of NCs

As the reciprocal lattice type of NCs belongs to a monoclinic system, the lattice type of the NC should belong to a monoclinic system. Here,  $A$ ,  $B$ , and  $C$  are lattice vectors of the NC,  $A$ ,  $B$ , and  $C$  are lattice constants of the NC, and  $\beta_{\text{NC}}$  is an angle between  $A$  and  $C$ . The unique axis is  $B//B^*$ .  $\beta_{\text{NC}}$  is defined as

$$\beta_{\text{NC}} \equiv \pi/2 + \psi + |\phi| \equiv \pi - \beta_{\text{NC}}^*. \quad (22)$$

From Eqs. 19, 21, and 22

$$\therefore \beta_{\text{NC}} = 104.7^\circ. \quad (23)$$

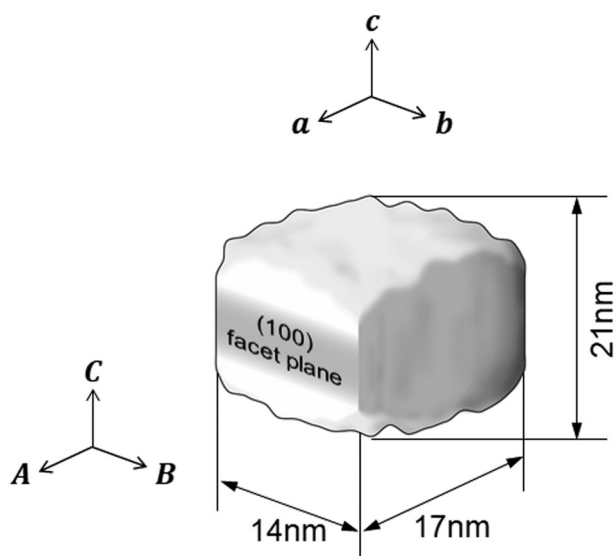


**Fig. 8** Schematic illustration of NC shape, with illustration of lattice vectors of the NC and unit cell. (Color figure online)

We obtained  $A$ ,  $B$ , and  $C$  using Bragg's equation from Figs. 3 and 7 as follows:

$$A \cong 2\pi/q(100), \quad (24a)$$

$$B \cong 2\pi/q(010) \quad (24b)$$

and

$$C \cong 2\pi/q(001), \quad (24c)$$

where  $q$  is a scattering vector and 100, 010, and 001 are indices in the SAXS image.  $q(hkl)$  was obtained from the peak of scattering intensity. Therefore, we obtained

$$A \cong 17 \text{ nm} \quad (25a)$$

$$B \cong 14 \text{ nm} \quad (25b)$$

and

$$C \cong 14 \text{ nm}. \quad (25c)$$

### Shape of an NC

As the NOCs of PET showed high crystallinity, we approximately obtained

$$d_A \cong A, \quad (26a)$$

$$d_B \cong B, \quad (26b)$$

and

$$d_C \cong C. \quad (26c)$$

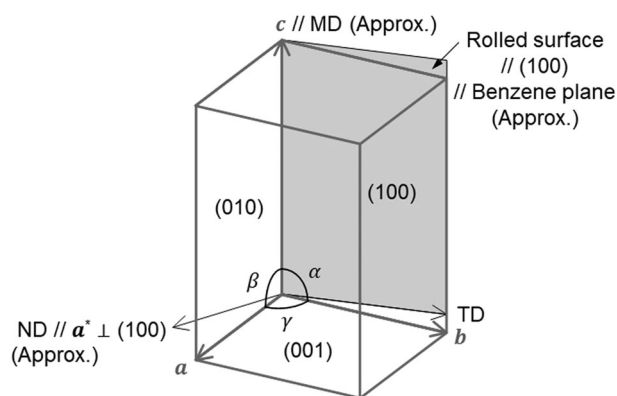


**Fig. 9** Schematic illustration of the relationship between the shape of a unit cell, rolled surface, and benzene plane. (Color figure online)

Therefore, from Eqs. 25 and 26, we obtained

$$d_A \cong 17 \text{ nm} \quad (27a)$$

$$d_B \cong 14 \text{ nm} \quad (27b)$$

and

$$d_C \cong 21 \text{ nm}. \quad (27c)$$

As the NCs are arranged in a paracrystal lattice,  $d_A$ ,  $d_B$ , and  $d_C$  should be of average size with a significant distribution.

We illustrate the shape of an NC in Fig. 8.

### Biaxial orientation of the unit cell

In WAXS patterns, the  $c$ -axis was parallel to MD, i.e.,  $c//MD$  (28) (Fig. 3d, e), while the  $a^*$ -axis was parallel to ND,  $a^*//ND$  (29) (Fig. 3e, f). Therefore, we concluded that the unit cell showed a biaxial orientation, which was the same as uniaxially drawn or rolled films of PET [14]. It is geometrically obvious that the rolled surface is perpendicular to ND, i.e., the rolled surface  $\perp ND$  (30). Hence, we obtain from Eqs. 29 and 30

$$(100)//\text{rolled surface}. \quad (31)$$

Here, (100) is a plane approximately parallel to the benzene plane [5]. Therefore, we concluded that the benzene plane is parallel to the rolled surface (Fig. 9).

### Formation mechanism of 3D structure and morphology

We show the 3D structure and morphology model of NOCs in Fig. 10. NCs were arranged in a monoclinic lattice. An NC appears to be a rectangular parallelepiped. The molecular chains are approximately oriented along MD.

We explain why the NOCs of PET showed a 3D structure and morphology as follows.

Step I: The morphology of the molecular chains should be a random coil in the supercooled isotropic melt for  $\dot{\epsilon} = 0 \text{ s}^{-1}$ .

Step II: When the supercooled melt was compressed and elongated in the condition  $\dot{\epsilon} > \dot{\epsilon}^*$ , portions of the molecular chains between entanglements were elongated, and the locally oriented melt should be realized [3]. Due to the hydrodynamic effect, the benzene plane should become parallel to the melt-elongational flow and be parallel to the rolled surface due to compression by a pair of rolls [15].

Step III: Aggregation of parallel-arranged benzene planes would become a precursor to a nucleus (hereafter called an “embryo”). The oriented melt and embryos should accelerate homogeneous nucleation and growth into NCs [4]. During nucleation and growth, (100) should be rearranged into a smooth surface, which results in the formation of “facets” (Fig. 8) [16]. NOCs will be formed with 3D structures and morphologies after overcoming entropy relaxation.

**Conclusions**

(1) We verified the formation of NOCs of PET using POM and X-ray observations. When  $\dot{\epsilon}$  exceeded  $\dot{\epsilon}^* = 1.5 \times 10^2 \text{ s}^{-1}$

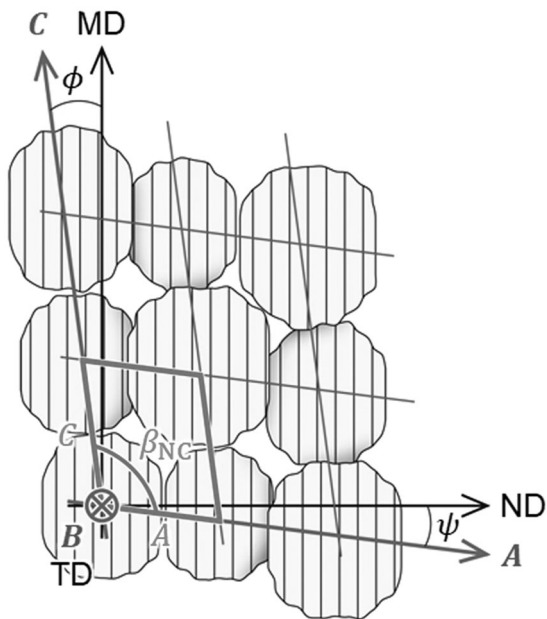


**Fig. 10** Schematic illustration of the 3D structure and morphology model of NOCs. NCs were arranged in a lattice-type monoclinic system. The molecular chains were approximately oriented along MD. (Color figure online)

**Fig. 11** Schematic illustration for formulation of  $\dot{\epsilon}$  in elongational crystallization of roll system. **a** Principle of the roll system. **b** Schematic illustration of  $\dot{\epsilon}_{xx}$  against  $x$ , which corresponds to **a**. (Color figure online)

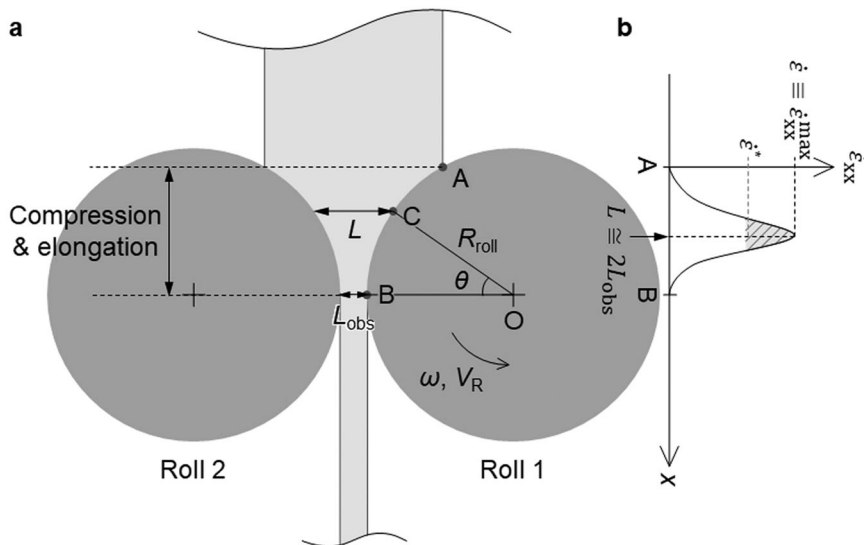


**Fig. 12** Schematic illustration of sample edge-view and SAXS patterns.  $T_c = 241 \text{ }^\circ\text{C}$  and  $\dot{\epsilon} = 3.2 \times 10^2 \text{ s}^{-1}$ . **a–c** X-ray was irradiated on the corresponding position in the sample. (Color figure online)



for  $T_c = 232\text{ }^\circ\text{C}$ , the structure and morphology discontinuously changed from FCCs to NOCs.

(2) The NOCs of PET showed a novel 3D structure and morphology. We clarified that NCs were arranged on a single crystal as a monoclinic lattice, which was a specific morphology for NOCs of PET. The shape of an NC was similar to a rectangular parallelepiped, where an NC can be regarded as a single crystal. The molecular chains were highly oriented along MD. The unit cell structure of NOCs was triclinic and showed a biaxial orientation. The (100) plane to which the benzene plane is approximately parallel was nearly parallel to the rolled surface.

(3) We clarified that the NOCs of PET showed high performance. The NOCs of PET showed a high heat resistance temperature ( $T_h$ )  $\cong 281\text{ }^\circ\text{C}$ , a high melting temperature ( $T_m$ )  $\cong 285\text{ }^\circ\text{C}$ , high maximum tensile stresses for MD and TD  $\cong 2.8 \times 10^2$  and 74 MPa, respectively, and high Young's moduli for MD and TD  $\cong 5.4$  and 1.7 GPa, respectively.

**Acknowledgments** The synchrotron radiation experiments were performed at BL03XU (Proposal Nos. 2014A7222, 2014B7272, 2015A7221, 2015B7273, 2016A7223, and 2016B7271) of SPring-8 with the approval of the JASRI. A part of this work was supported by Grants-in-Aid for Scientific Research of the Japan Society for the Promotion of Science (KAKENHI No.26410222). We thank M. Hikosaka and S. Hikosaka, Hiroshima University, for assistance in experiments.

## Compliance with ethical standards

**Conflict of interest** The authors declare that they have no competing interests.

## APPENDIX

### Formulation of $\dot{\epsilon}$ in elongation of the melt by rolls

We will formulate  $\dot{\epsilon}$  in the compression and elongation using the roll system. We focus on a range from the start (position A) to the end (position B) of compression and elongation of the supercooled melt (Fig. 11a). Hereafter, we refer to this as "range AB". Here, O is the center of Roll 1,  $\omega$  is angular velocity,  $L$  is the thickness of the supercooled melt at any given position in the range AB and  $L_{\text{obs}}$  is the thickness of the sheet at position B.  $\theta$  is an angle of  $\angle\text{COB}$ ,

$$\theta \ll 1 \quad (\text{A1})$$

$$R_{\text{roll}} \gg L_{\text{obs}} \quad (\text{A2})$$

We consider a microvolume ( $\phi_{\text{vol}}$ ) at any given position in the range AB, consider an origin at the center of  $\phi_{\text{vol}}$ , and take the  $x$ -axis,  $y$ -axis, and  $z$ -axis along MD, TD, and ND, respectively. We approximate  $\phi_{\text{vol}}$  with a rectangular parallelepiped, and each lateral length of  $\phi_{\text{vol}}$  is  $x$ ,  $y$ , and  $L$ . As

the width of a sheet  $y$  is large enough compared to  $x$  and  $L$ ,  $y$  does not change during compression and elongation of the supercooled melt, i.e.,  $y \cong \text{const} \gg x, L$  (A3). Therefore, the supercooled melt should be compressed along the  $z$ -axis and elongated along the  $x$ -axis in the elongational crystallization via the roll system.

It is obvious that the tensor component of  $\dot{\epsilon}$  along the  $x$ -axis ( $\dot{\epsilon}_{xx}$ ) and  $z$ -axis ( $\dot{\epsilon}_{zz}$ ) should satisfy the following relationship,

$$\dot{\epsilon}_{xx} = -\dot{\epsilon}_{zz} \quad (\text{A4})$$

based on Eq. A3 and the mass conservation law with respect to  $\phi_{\text{vol}}$ ,  $\phi_{\text{vol}} \cong xyL = \text{const}$  (A5). Here,  $\dot{\epsilon}_{zz}$  is defined by

$$\dot{\epsilon}_{zz} \equiv \frac{1}{L} \cdot \frac{dL}{dt}, \quad (\text{A6})$$

where  $t$  is time.

From Fig. 11a,  $L$  is written as

$$L = 2R_{\text{roll}}(1 - \cos\theta) + L_{\text{obs}}. \quad (\text{A7})$$

Since  $\cos\theta$  is approximated by  $\cos\theta \cong 1 - \frac{1}{2}\theta^2$  (A8) from Eq. A1, we can obtain, using Eqs. A7 and A8,

$$L = R_{\text{roll}}\theta^2 + L_{\text{obs}}. \quad (\text{A9})$$

$$\therefore \theta = \left( \frac{L - L_{\text{obs}}}{R_{\text{roll}}} \right)^{1/2} \quad (\text{A10})$$

Here,  $\omega \equiv -\left(\frac{d\theta}{dt}\right)$  (A11) and  $\omega = V_R/R_{\text{roll}}$  (A12). From Eqs. A4, A6, A9, A10, and A11, we have

$$\dot{\epsilon}_{xx} \cong 2\omega \sqrt{\frac{R_{\text{roll}}}{L} \left( 1 - \frac{L_{\text{obs}}}{L} \right)}. \quad (\text{A13})$$

As  $\dot{\epsilon}_{xx}$  has a maximum ( $\dot{\epsilon}_{xx}^{\text{max}}$ ) at  $L = 2L_{\text{obs}}$  (A14), from Eqs. A13 and A14, we obtain

$$\therefore \dot{\epsilon}_{xx}^{\text{max}} \cong \omega \sqrt{\frac{R_{\text{roll}}}{L_{\text{obs}}}}. \quad (\text{A15})$$

To form NOCs (Fig. 11b), it is a necessary condition that  $\dot{\epsilon}_{xx}^{\text{max}}$  is larger than  $\dot{\epsilon}^*$ .

Here, we define Eq. A15 as  $\dot{\epsilon}$ , i.e.,  $\dot{\epsilon} \equiv \dot{\epsilon}_{xx}^{\text{max}}$  (A16). Therefore, from Eqs. A12, A15, and A16, we can obtain

$$\therefore \dot{\epsilon} = \frac{V_R}{\sqrt{R_{\text{roll}}L_{\text{obs}}}}. \quad (\text{A17})$$

### Inclined two-point patterns in SAXS patterns for edge-view

We observed the inclined two-point pattern of 100 with an angle of  $\pm\phi$  in the SAXS pattern for the edge-view (Fig. 12). The dominant inclined two-point patterns in Fig. 12a, c were asymmetric and mirrored one another. In contrast, the image of b shows a symmetric pattern. Therefore, the monoclinic arrangement of NCs, shown in DISCUSSION, partly showed an inside-out pattern with low probability.

## References

1. Okada K, Washiyama J, Watanabe K, Sasaki S, Masunaga H, Hikosaka M. Elongational crystallization of isotactic polypropylene forms nano-oriented crystals with ultra-high performance. *Polymer J.* 2010;42:464–73.
2. Kakudo M, Kasai N. *Kobunshi xsen kaisetsu*. Tokyo, Japan: Maruzen publishing Co. Ltd.; 1968. p. 75–96.
3. Okada K, Tagashira K, Sakai K, Masunaga H, Hikosaka M. Temperature dependence of crystallization of nano-oriented crystals of iPP and the formation mechanism. *Polymer J.* 2013;45:70–8.
4. Price FP. Nucleation. In: Zettlemoyer AC, editor. Ch. 8. New York, NY: Marcel Dekker Inc.; 1969.
5. Daubeny R, de P, Bunn CW, Brown CJ. The crystal structure of polyethylene terephthalate. *Proc R Soc Lond.* 1954;A226:531–42.
6. Ikeda M, Mitsuishi Y. Studies on thermal behavior and fine structure of polyethylene-terephthalate. I. Equilibrium melting temperature and surface free energy. *Kobunshi Kagaku.* 1967;24:378–84.
7. Fakirov S, Fischer EW, Hoffmann R, Schmidt GF. Structure and properties of poly(ethylene terephthalate) crystallized by annealing in the highly oriented state: 2. Melting behavior and the mosaic block structure of the crystalline layers. *Polymer.* 1977;18:1121–9.
8. Mehta A, Gaur U, Wunderlich B. Equilibrium melting parameters of poly(ethylene terephthalate). *J Polymer Sci Polymer Phys.* 1978;16:289–96.
9. Dörscher M, Wegner G. Poly(ethylene terephthalate): a solid state condensation process. *Polymer.* 1978;19:43–7.
10. Alexander LE. X-ray diffraction methods in polymer science. Ch. 4. Kyoto, Japan: Kagaku-Dojin Publishing Company Inc.; 1973.
11. Hahn T, editor. *International tables for crystallography*. Vol. A. 4th ed. Dordrecht, Netherlands: Kluwer Academic Publishers; 1996. p. 106–7.
12. Asano T, Seto T. Morphological studies of cold drawn poly(ethylene terephthalate). *Polymer J.* 1973;5:72–85.
13. Kan-no T. *Plastics processing databook*. Tokyo, Japan: Nikkan Kogyo Shimbun, The Japan Society for Technology of Plasticity; 2002. p 39.
14. Fischer EW, Fakirov S. Structure and properties of polyethyleneterephthalate crystallized by annealing in the highly oriented state. Part 1 Morphological structure as revealed by small-angle X-ray scattering. *J Mater Sci.* 1976;11:1041–65.
15. Tatsumi T. *Ryutairikigaku*. Tokyo, Japan: Baifukan Co. Ltd.; 1982. p. 171.
16. Kassner K. Science and technology of crystal growth. In: van der Eerden JP, Bruinsma OSL, editors. Dordrecht, Netherlands: Kluwer Academic Publishers; 1995. p. 193.